

Topographic Control of Basin and Channel Flows: The Role of Bottom Pressure Torques and Friction

LAURA JACKSON*

Department of Earth and Ocean Sciences, University of Liverpool, Liverpool, United Kingdom

CHRIS W. HUGHES

Proudman Oceanographic Laboratory, Liverpool, United Kingdom

RICHARD G. WILLIAMS

Department of Earth and Ocean Sciences, University of Liverpool, Liverpool, United Kingdom

(Manuscript received 31 July 2004, in final form 24 January 2006)

ABSTRACT

The topographical control of western boundary currents within a basin and zonal jets in a channel is investigated in terms of the potential vorticity (PV) and barotropic vorticity (BV: the curl of the depth-integrated velocity) budgets using isopycnic, adiabatic wind-driven experiments. Along the western boundary, the wind-driven transport is returned across latitude lines by the bottom pressure torque, while friction is only important in altering the PV within an isopycnic layer and in allowing a closed circulation. These contrasting balances constrain the geometry of the flow through integral relationships for the BV and PV. For both homogenous and stratified basins with sloping sidewalls, the northward subtropical jet separates from the western wall and has opposing frictional torques on either side of the jet, which cancel in a zonal integral for BV but alter the PV within a layer streamline. In a channel with partial topographic barriers, the bottom pressure torque is again important in returning wind-driven flows along western boundaries and in transferring BV from neighboring wind-driven gyres into a zonal jet. The depth-integrated flow steered by topography controls where the bottom friction alters the PV, which can lead to different PV states being attained for separate subbasins along a channel.

1. Introduction

There is an apparent paradox concerning the role of friction in the wind-driven ocean circulation. On the one hand, it is widely accepted that friction is important for the potential vorticity (PV) budget and in ensuring a closed circulation. On the other hand, friction is viewed as unimportant in enabling the return flow of the wind-driven transport in western boundary currents when there are sloping sidewalls, as has been shown for

the zonal integral of the barotropic vorticity (the curl of the depth-integrated velocity) balance; see theoretical arguments (Hughes 2000) and model diagnostics for a realistic ocean (Hughes and de Cuevas 2001, hereinafter HdC). This barotropic vorticity (BV) balance is the generalization of Sverdrup balance, which is at the heart of the oceanographer's understanding of how ocean gyres function.

The fact that friction is important in one balance but not in the other is not in itself surprising. However, the study of wind-driven circulation has in the past been dominated by theory based on models with flat bottoms and vertical sidewalls. For this special case, in a single-layer model, the BV and PV equations are the same, so friction must be equally important in either. Our aim is to clarify how the constraints imposed by these two different equations evolve as the representation of the ocean changes from a single-layer gyre with topogra-

* Current affiliation: Geophysical Fluid Dynamics Laboratory, Princeton, New Jersey.

Corresponding author address: Dr. R. G. Williams, Department of Earth and Ocean Sciences, University of Liverpool, Liverpool L69 3GP, United Kingdom.
E-mail: ric@liv.ac.uk

phy, to a stratified gyre with topography, and finally to a stratified channel with topography.

The PV and BV equations can be written, for a stratified ocean with bottom topography, as

$$\rho h \frac{D}{Dt} \left(\frac{f + \zeta}{h} \right) = \mathbf{k} \cdot \nabla \times \left(\frac{\Delta \boldsymbol{\tau}}{h} \right), \quad (1)$$

and

$$\beta V = J(p_b, H) + \mathbf{k} \cdot \nabla \times (\boldsymbol{\tau}_w - \boldsymbol{\tau}_b + \mathbf{A}). \quad (2)$$

Here, in (1), D/Dt is the Lagrangian rate of change, $Q = (f + \zeta)/h$ is referred to as the PV, f is the planetary vorticity and β its northward derivative, ζ is the vertical component of relative vorticity, h is a layer thickness, and $\Delta \boldsymbol{\tau}$ represents the difference between viscous stresses on the top and bottom of the layer. In (2), with η as the sea surface elevation, the depth-integrated northward mass flux is $V = \int_{-H}^{\eta} \rho v \, dz$, $\boldsymbol{\tau}_w$ and $\boldsymbol{\tau}_b$ are surface wind stress and bottom stress, respectively, and \mathbf{A} represents nonlinear vorticity advection. The bottom pressure torque is represented by $J(p_b, H)$, where p_b is the pressure at the sea floor, H is ocean depth, the Jacobian is defined by

$$J(A, B) = \frac{\partial A}{\partial x} \frac{\partial B}{\partial y} - \frac{\partial A}{\partial y} \frac{\partial B}{\partial x},$$

and \mathbf{k} is a unit vector in the local vertical (upward).

Some assumptions have been made in these equations, appropriate to the model investigations presented later: lateral friction has been neglected since its effects are much smaller than those of the bottom stress in our model results, although its effect can be easily incorporated if required; time dependence has been neglected in (2) since a statistically steady state is considered; and, perhaps most importantly, the effect of diapycnal fluxes has been neglected from the right-hand side of (1). This latter choice is to ensure that any wind stress forcing in (1) cannot be balanced by the diapycnal transfer, thus requiring friction to be important.

a. Barotropic vorticity and potential vorticity balances

The PV and BV balances, (1) and (2), become identical for a single-layer, flat-bottomed ocean with $h = H = \text{const}$, and $\Delta \boldsymbol{\tau} = \boldsymbol{\tau}_w - \boldsymbol{\tau}_b$. From this limit is derived the canonical picture of a gyre with an interior in Sverdrup balance, $\beta V = \mathbf{k} \cdot \nabla \times (\boldsymbol{\tau}_w)$, such that the flow across f contours is forced by wind stress curl, and friction is required in a narrow boundary current to permit the required return flow across $f + \zeta$ contours to close the gyre.

In more realistic circumstances including topography

and stratification, the bottom pressure torque becomes important in the BV balance constraining the meridional transport across latitude circles. Conversely, the PV balance only constrains flow across PV contours, which can be substantially nonzonal, and meridional flows can occur locally without any corresponding change in PV. As we shall see in the following sections, the BV equation retains some capability to constrain the geometry of the flow, while the PV equation is useful in constraining the flow within closed streamlines and as a Lagrangian diagnostic. Together, the two equations provide strong constraints on the flow in many circumstances.

b. Interpretation of the bottom pressure torque

Given the importance of the bottom pressure torque $J(p_b, H)$ in allowing meridional flows (see Holland 1973; HdC), it is worth giving a brief physical interpretation. The bottom pressure torque arises from the variation of bottom pressure p_b along isobaths. The weight of overlying fluid at the seafloor always creates an equal and opposite pressure force from the topography into the ocean. When there is sloping topography, this normal pressure force has a horizontal component, as well as a vertical component. If this horizontal component of the normal pressure force changes with distance along the isobath, then a “twisting force” or (informally) a bottom pressure torque is exerted on the vertical cylinder of the overlying fluid. This bottom pressure torque is exactly analogous to that exerted by the wind stress curl at the surface. In addition, both bottom pressure torque and wind stress curl can be considered in terms of vertical velocities. While wind stress curl induces an Ekman pumping at the base of the Ekman layer, bottom pressure torque can be interpreted in terms of the geostrophic flow at the sea floor. At the seafloor, $\rho f \mathbf{u}_b = (\mathbf{k} \times \nabla p)_b$, so that $\rho f \mathbf{u}_b \cdot \nabla H = J(p_b, H)$. As there is no flow through the seafloor, any horizontal flow toward an isobath must be accompanied by a vertical flow, so the flow will be upslope, giving the kinematic boundary condition $w_b = -\mathbf{u}_b \cdot \nabla H$, from which we see that $\rho f w_b = -J(p_b, H)$. When friction is allowed, this becomes a condition at the top of the bottom Ekman layer, and the effect of bottom stress curl must also be allowed.

The one major difference between bottom pressure torque and wind stress curl is that bottom pressure torque is determined dynamically by the ocean rather than being externally imposed. There is no energy input or dissipation associated with the bottom pressure torque, and it affects only the mass transport and BV but not the PV of the fluid. For this reason, it is incorrect to view the bottom pressure torque as driving the

flow, it can only be in balance with a particular flow and is a measure of the topographic steering of the flow.

Another way to interpret the bottom pressure torque is to consider its relationship to flow along f/H contours. In an unforced, barotropic basin in the absence of inertial effects the streamlines lie along f/H contours, and the BV Eq. (2) reduces to $\beta V = J(p_b, H)$. Hence the bottom pressure torque arises in order to balance a meridional flow such that the streamfunction is directed along f/H contours.

Our study now focuses on two questions: 1) How are the BV and PV balances reconciled in simple ocean geometries and 2) is the role of the bottom pressure torque simply to steer the flow or does it have a broader, perhaps indirect, dynamical influence on the flow? We address these questions in the context of an ocean gyre circulation and a channel with topography.

2. Gyre circulations

a. Model formulation

The model experiments focus on the dynamical control of the depth-integrated transport for a basin following the barotropic study of Becker and Salmon (1997). A layered, isopycnic model, the Miami Isopycnic Coordinate Ocean Model (MICOM 2.6; Bleck and Smith 1990), is employed with grid size $1/2^\circ$ in a rectangular basin of dimensions 40° latitude by 20° longitude. A zonal, sinusoidal wind stress is applied over the middle 20° latitude of the basin,

$$\tau_w^x = \begin{cases} 0, & 40^\circ < y \leq 50^\circ \\ \tau_0 \left\{ 1 - \cos \left[\frac{2\pi(40 - y)}{20} \right] \right\} & 20^\circ \leq y \leq 40^\circ \\ 0, & 10^\circ \leq y < 20^\circ, \end{cases}$$

where $\tau_0 = 0.1$ Pa and the superscript x denotes the eastward component. A bottom drag is applied with stress given by $\tau_b = -\rho c_D (|\mathbf{u}_b| + c_{\text{ref}}) \mathbf{u}_b$, where \mathbf{u}_b is the bottom velocity, c_D is the bottom drag coefficient, and $c_{\text{ref}} = 10 \text{ cm s}^{-1}$ is a reference velocity. The bottom Ekman layer structure is imposed by reducing the stress to zero 10 m above the ocean floor. The effect of sub-grid-scale viscous processes is parameterized using a biharmonic diffusion, producing a viscous acceleration \mathbf{D} given by

$$\mathbf{D} = -\frac{1}{h} \nabla \cdot [v h \nabla (\nabla^2 \mathbf{u})], \quad (3)$$

where the viscosity ν is given by

$$\nu = \Delta x^3 \max \left\{ u_d, \lambda \left[\left(\frac{\partial u}{\partial x} - \frac{\partial v}{\partial y} \right)^2 + \left(\frac{\partial v}{\partial x} + \frac{\partial u}{\partial y} \right)^2 \right]^{1/2} \right\} \Delta x, \quad (4)$$

with the parameters $u_d = 1 \text{ cm s}^{-1}$ and $\lambda = 0.2$; Δx is the grid size. Lateral boundary conditions of no normal flow through the boundary and free slip along the boundary are applied to both \mathbf{u} and $\nabla^2 \mathbf{u}$. Mathematically, if $\hat{\mathbf{s}}$ is the unit vector tangential to the boundary and $\hat{\mathbf{n}}$ is the unit vector normal, then $\mathbf{a} \cdot \hat{\mathbf{n}} = 0$ and $\partial(\mathbf{a} \cdot \hat{\mathbf{s}})/\partial \hat{\mathbf{n}} = 0$ are applied where \mathbf{a} represents \mathbf{u} and $\nabla^2 \mathbf{u}$ on the boundary.

The bottom topography is chosen to vary in a simple manner, deepening from a shallow shelf along the western and eastern walls following a Gaussian form, $H(x) = 100 + (H_i - 100)[1 - e^{-x^2} - e^{-(x_0 - x)^2}]^{1/2}$ (m), where x is the longitude and x_0 is the width of the basin in degrees. The interior depth H_i is taken as 1400 m in the barotropic case and 4000 m in the baroclinic case. The model integrations were spun up to a statistically steady state (15 yr for the barotropic runs, and 25 yr for the baroclinic runs), and results given for a time average taken over the next 5 yr.

Two sets of basin experiments are conducted:

- 1) *Barotropic gyre experiments.* The model is chosen to have only two layers and the interface is strongly relaxed toward 100 m, such that the upper layer acts as a surface Ekman layer. This configuration is chosen to separate the layers in which the wind stress and bottom drag are applied, but otherwise is effectively barotropic. Both frictional and inertial limits are investigated by altering the drag coefficient for bottom friction, c_D , from 8×10^{-3} to 8×10^{-4} . Vertical sidewall cases were also run and, as expected, found to replicate the classical Stommel (1948) and Fofonoff (1954) solutions.
- 2) *Baroclinic gyre experiments.* The frictional and inertial limits are again investigated using $c_D = 8 \times 10^{-3}$ and 8×10^{-4} in a five-layer baroclinic model. The maximum basin depth was increased to 4000 m to prevent intermediate layers from outcropping at the surface or grounding (other than along the sidewalls). The initial depths of the lower-layer interfaces were set to 500, 1250, 2000, 2750, and 4000 m and the density as 1027.7, 1028.8, 1028.9, 1029.0, and 1029.1 kg m^{-3} so that the lower layers are weakly stratified. The top layer acts again as an Ekman layer with the interface between the first two layers being strongly relaxed to its initial depth. All layers experience bottom friction where they interact with

the topography over the sloping walls. The interior (third and fourth) layers experience no forcing in the interior (apart from eddy stirring and lateral friction) away from the narrow bands of frictional forcing where they interact with topography.

b. Barotropic vorticity balance

1) HOW DOES FLUID MOVE MERIDIONALLY IN BOUNDARY CURRENTS?

The flow pattern and the balance of terms in the BV Eq. (2) are now explored for high and low friction in both barotropic and baroclinic experiments.

The classical case of barotropic flow and vertical sidewalls is well known: a Stommel (1948) solution for high friction, with the interior wind-driven flow returned in a frictionally controlled boundary current, and a Fofonoff (1954) solution for low friction, with an eastward jet along the center of the basin bounded by inertial recirculations.

For sloping sidewalls, there is a wind-driven interior in Sverdrup balance, as in the vertical sidewall case, but the western boundary region differs significantly. There is an equatorial convergence of f/H contours along the western slope, which leads to a corresponding distortion of the streamlines (Fig. 1) as predicted by linear theory (Welander 1968). The western boundary flows are now not pinned to the western wall of each gyre, but instead lie together along the slope broadly following f/H contours. This general pattern is robust, occurring in both frictional and inertial limits, for both barotropic and baroclinic gyres. As the friction is reduced or as we move to the baroclinic limit, the jet becomes narrower and stronger and inertial recirculations develop. This is also seen in the barotropic solutions of Becker and Salmon (1997). In the frictional limit of baroclinic solutions, the stratification allows a weaker deep flow over the topography which results in less influence of f/H contours on the streamfunction in Fig. 1c.

The total meridional transport in the boundary current is balanced by the bottom pressure gradient torque, as revealed by zonal sections of the terms in (2) in Fig. 2 and in accord with the model diagnostics of HdC. However, friction and inertia can alter the detail of the boundary current. Friction provides an anticyclonic torque on the shoreward side of the jet center where there is cyclonic vorticity and, conversely, a cyclonic torque offshore of the jet center (Fig. 2a). This frictional torque acts in opposition to the bottom pressure torque, shoreward of the jet center and in concert with bottom pressure torque offshore of the jet center, the net effect of the friction being to displace the jet

offshore of the position suggested by the bottom pressure torque.

The inertial and baroclinic cases (Figs. 2b–d) are very similar, but with the nonlinear term also becoming important, particularly in the inertial case as the jet narrows and the scale decreases at which friction becomes effective. The nonlinear term also has a reversing sign and is important in balancing the oscillations in flow direction offshore, as in inertial recirculations. Within the main jet, the detailed interaction between nonlinear and frictional terms is rather complicated, but their net effect remains the same: to move the jet offshore rather than to balance the net meridional transport in the jet. We note that, in the frictional, baroclinic case, the bottom pressure torque is still the dominant term balancing a meridional flow (Fig. 2c) despite the apparent reduction of topographical steering seen in the streamfunction (Fig. 1c).

2) HOW DO THE PATTERNS OF BOTTOM PRESSURE TORQUE AND FRICTION VARY?

To show how these balances translate to other latitudes, we consider the patterns of bottom pressure torque and frictional torque along the western region of the domain, for the four model cases in Figs. 3 and 4, with the barotropic streamfunction superimposed. Although details of the flow patterns vary, in all cases the bottom pressure torque reflects meridional flow along the slope (Fig. 3): there is a characteristic dipole pattern for bottom pressure torque with positive and negative regions respectively along the subtropical and subpolar gyres. This is consistent with the results, seen in Fig. 2, that the meridional flow is predominantly balanced by the bottom pressure torque. In the baroclinic cases, the role of the bottom pressure torque in balancing a meridional flow remains clear, even though the influence of f/H contours on the streamfunction becomes less obvious (Fig. 3c).

For the subpolar gyre, friction is unimportant in what would traditionally be considered the western boundary current where southward flow occurs along the continental slope (Fig. 4a). Significant friction, instead, only occurs in the northward flow alongside the subtropical gyre. Instead of friction occurring along the western boundary, it now takes opposite signs on either side of the jet, consistent with vorticity patterns, and its associated length scale becomes smaller as the jet narrows in response to baroclinicity and reduction of friction (Figs. 4b–d). In the frictional, baroclinic solution (Fig. 4c) there are regions of significant friction away from the jet. This is consistent with strong meridional flow along the boundary; however, there are still re-

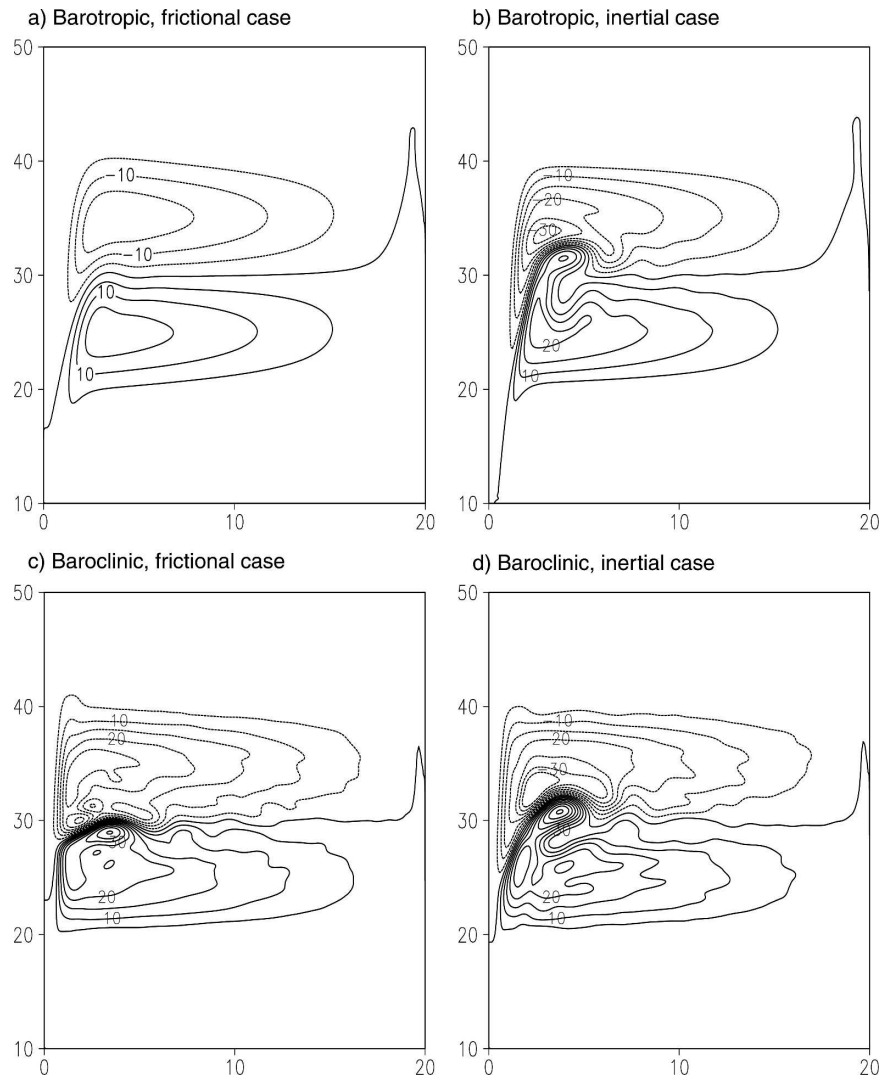


FIG. 1. The streamfunction, Ψ ($Sv \equiv 10^6 \text{ m}^3 \text{ s}^{-1}$), for the following gyre integrations with sloping sidewalls: (a) barotropic frictional, (b) barotropic inertial, (c) baroclinic frictional, and (d) baroclinic inertial. The Ψ pattern reveals a western jet running from the equator along the slope to the intergyre boundary, which remains broadly unchanged as the friction and stratification alters. The slope is typically 2° wide.

gions of both positive and negative forcing at each latitude.

The sign of the frictional term in Fig. 4 does not reflect the direction of the separated jet across f contours since there is a northward flow where there is a negative frictional term on the shoreward (cyclonic) side of the jet. Instead, the friction is controlling how fluid moves across f/H contours with negative and positive forcing driving fluid to lower or higher f/H contours, respectively.

There is a clear contrast between all of these experiments and the classical vertical sidewall case. In a Stommel boundary layer, the viscous torque balances

the meridional motion (with a positive vorticity input in the subtropical gyre and negative input in the subtropical gyre) and bottom pressure torque confined to a delta function at the sidewalls (HdC). In the experiments with sloping sidewalls, the bottom pressure torque instead balances the meridional flow, with the frictional torque occurring in a dipole on either side of the jet center and, therefore, integrating zonally to zero.

c. Integral constraints for the circulation

These patterns of bottom pressure torque and frictional forcing solve the apparent paradox regarding the

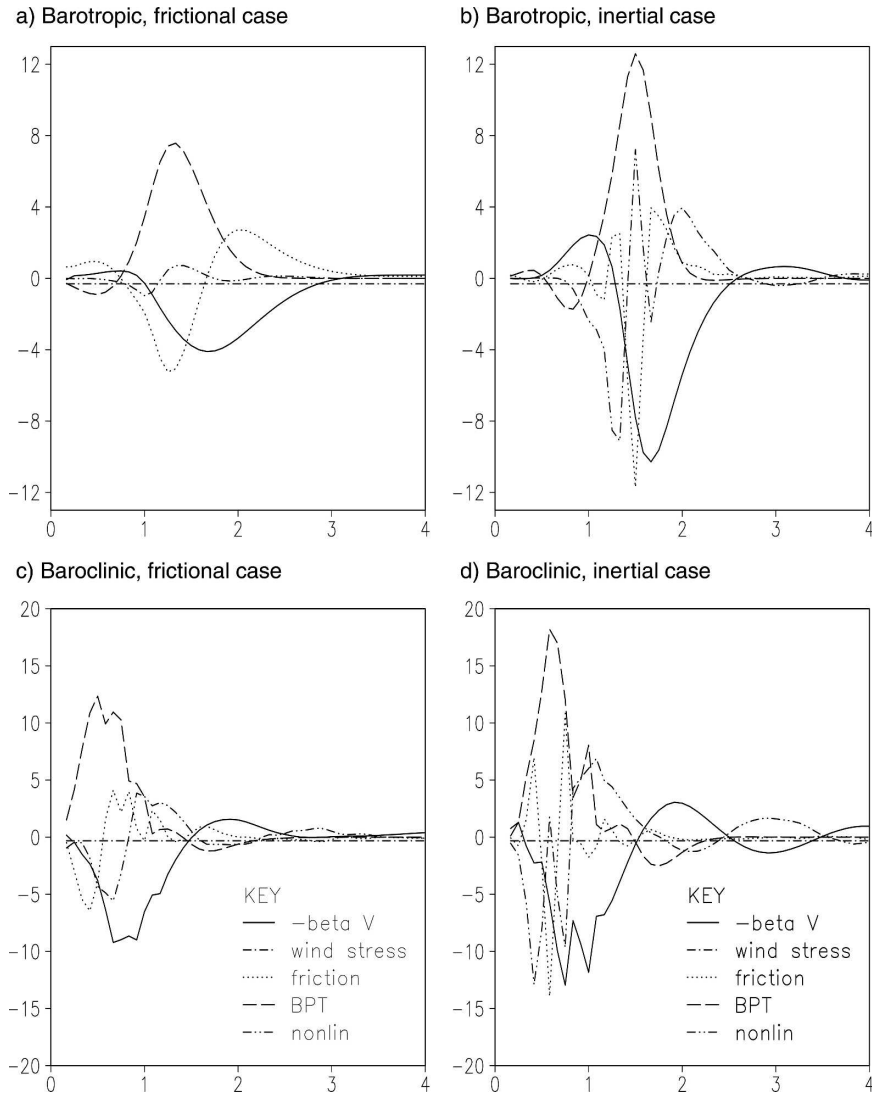


FIG. 2. Cross-sectional balances in the depth-integrated barotropic vorticity equation (10^{-9} m s^{-2}) at 25°N through the subtropical gyre for the following gyre integrations: (a) barotropic frictional, (b) barotropic inertial, (c) baroclinic frictional, and (d) baroclinic inertial. In (a), the northward transport (full line for $-\beta V$) is controlled by bottom pressure torque (dashed line), rather than by friction, which reverses sign across the jet (dotted line). These balances broadly carry over for the inertial cases [(b)] and the baroclinic cases [(c) and (d)] but with additional nonlinear, eddy transfers (dash-dot-dot line). Note that the x axis is stretched to show the detail of the western boundary region.

role of friction discussed in the introduction. This is most clearly shown by comparing the BV equation with the PV equation for an adiabatic layer forced by wind. If we consider a statistically steady state and a layer with no mass sources or sinks, then we can introduce a mass transport streamfunction ψ for the layer such that $\overline{\rho \mathbf{u}}/h = \mathbf{k} \times \nabla \psi$. The time-averaged PV Eq. (1) can then be written as

$$J(\psi, \overline{Q}) = \mathbf{k} \cdot \nabla \times \left(\frac{\Delta \tau}{h} \right) - \nabla \cdot [\overline{\rho(h\mathbf{u})'Q'}], \quad (5)$$

where an overbar denotes a time average and a prime denotes a difference from the time average. The need for friction to balance the PV input due to wind stress can then be seen by applying this equation to the top layer and integrating over an area bounded by a streamline ψ_0 , to give

$$\int_{\text{inside } \psi_0} \mathbf{k} \cdot \nabla \times \left(\frac{\Delta \tau}{h} \right) dA = \int_{\text{inside } \psi_0} \nabla \cdot [\overline{\rho(h\mathbf{u})'Q'}] dA, \quad (6)$$

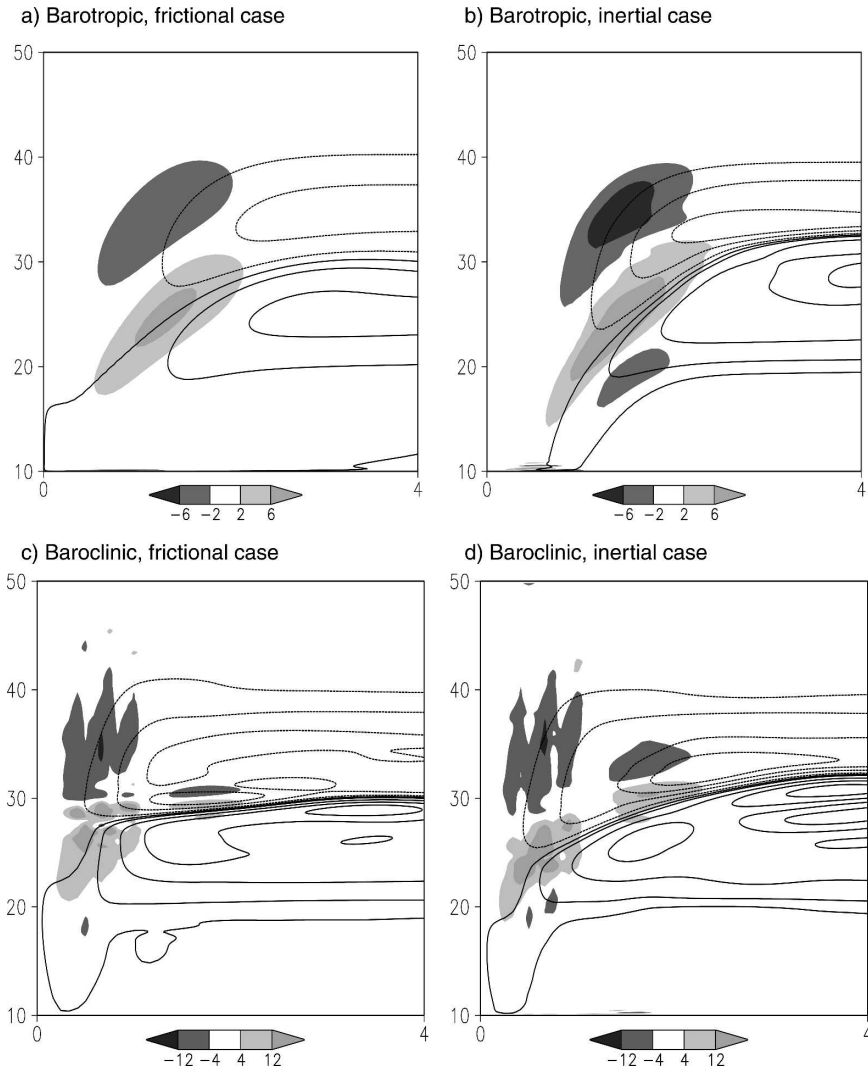


FIG. 3. Maps of bottom pressure torque (10^{-9} m s^{-2}) with streamlines of contour interval 10 Sv overlaid for the following gyre integrations: (a) barotropic frictional, (b) barotropic inertial, (c) baroclinic frictional, and (d) baroclinic inertial. A positive sign indicates a flow from low to high f with the northward flow in the jet due to a positive bottom pressure torque. Note that the x axis is stretched to show details of the western boundary region with the slope typically 2° wide.

where $\Delta\tau = \tau_w$, except where the layer intersects topography, where $\Delta\tau = \tau_w - \tau_b$. Applying Stokes's theorem, we see that τ_w/h must be balanced by bottom stress along each streamline and eddy PV fluxes across the streamline.

Similarly, if the BV Eq. (2) is rewritten in the form

$$\nabla \cdot (\mathbf{U}f) = \mathbf{k} \cdot \nabla \times (p_b \nabla H + \tau_w - \tau_b + \mathbf{A}), \quad (7)$$

where $\mathbf{U} = \int_{-H}^{\eta} \rho \mathbf{u} dz$ is the depth-integrated mass transport, then we can integrate this over a zonal strip of ocean; an area bounded by the contour δ consisting of two latitude lines and two sections of coastline.

Since, for a closed basin, the total mass flux across each latitude line is zero, the left-hand side integrates to zero, leaving

$$\int_{\text{inside } \delta} \mathbf{k} \cdot \nabla \times (p_b \nabla H + \tau_w - \tau_b + \mathbf{A}) dS = 0. \quad (8)$$

This balance has been shown by HdC to be dominated by the wind stress and pressure terms, with bottom friction negligible, and the nonlinear term important only for strips much narrower than an ocean gyre.

Therefore, friction or eddies must balance τ_w/h along

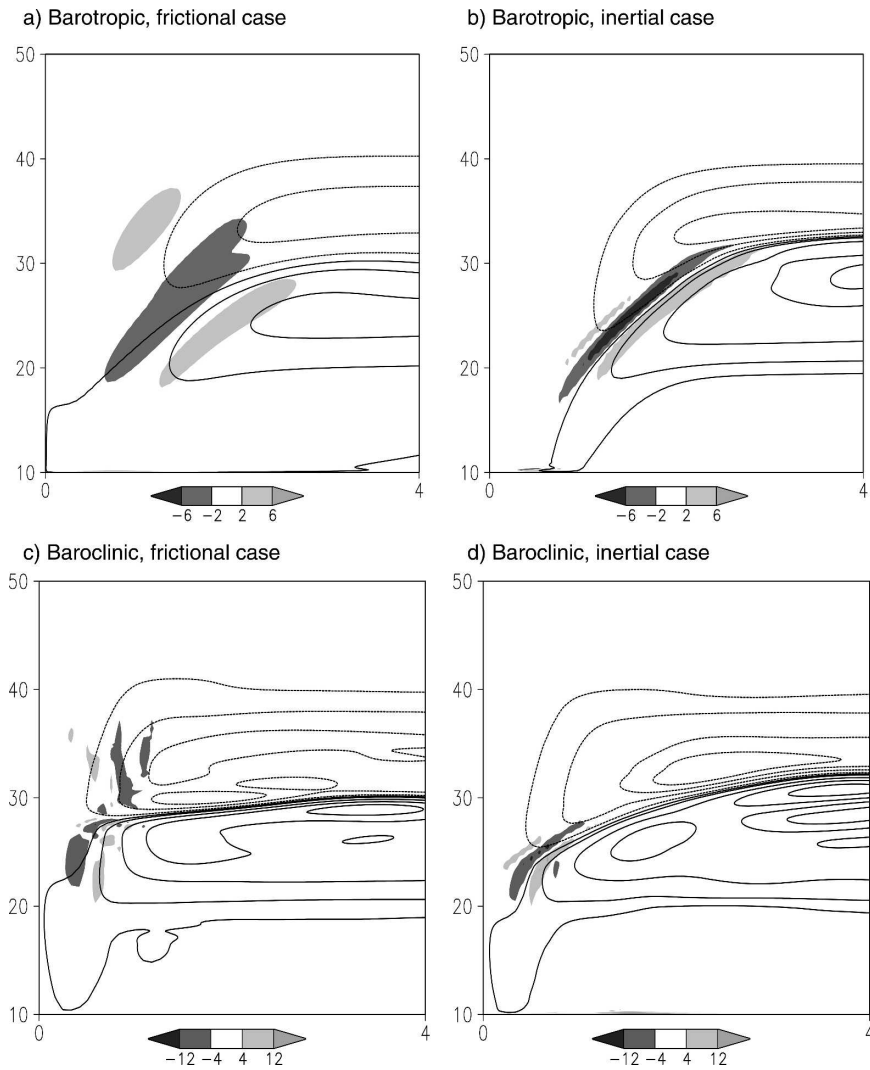


FIG. 4. Maps of frictional terms (10^{-9} m s^{-2}) in the barotropic vorticity balance with streamlines of contour interval 10 Sv overlaid for the following gyre integrations: (a) barotropic frictional, (b) barotropic inertial, (c) baroclinic frictional, and (d) baroclinic inertial. A positive sign indicates a flow from low to high f/H contours due to frictional forcing. Note that the x axis is stretched to show details of the western boundary region with the slope typically 2° wide.

any closed streamline in (6), but their effects are much smaller than wind stress and bottom pressure terms when integrated along latitude lines in (8). One way for this to happen might be for the bottom stress to occur in very shallow water, producing a large value of $\Delta\tau/h$ in (6) while only retaining a small contribution to τ_b in (8), but that can only work for streamlines that pass into shallow water. As seen in the model diagnostics, the alternative is that bottom stress torques become large in the jet and for any integral along a closed streamline, but situated so that there is only a small contribution to the zonal integral (with an anticyclonic

torque to the left of the jet center and a cyclonic torque to the right).

In order for the PV constraint to be realized, water from the subpolar gyre, where wind stress forcing is cyclonic, must pass through the left-hand side of the jet (cyclonic side), and water from the subtropical gyre must pass through the right-hand side of the jet (anticyclonic side). When the jet is guided along f/H contours and remains separated from the western boundary, this constraint results in the asymmetrical circulation pattern seen in the model results. In particular, a branch of the subpolar gyre has to penetrate southward

in order to join the cyclonic side of the jet as it flows northward.

Although this balance has been demonstrated in a system for which bottom friction is a dominant term in the PV budget, we would expect similar results with either lateral friction or eddy PV transport as the dominant term since the effect of friction is to damp the vorticity and reduce the PV difference across the jet (where water on the left-hand side of the jet is of subpolar origin and water on the right-hand side of the jet center is of subtropical origin). Either lateral viscosity or eddy mixing could have a similar effect.

Our model diagnostics reveal that these contrasting integral constraints are achieved through the separation of the subtropical jet and the associated southward penetration of the western boundary current from the subpolar gyre across the intergyre boundary (as defined by the wind stress curl forcing). The strong northward-flowing jet then has subtropical water on its eastward side and subpolar water on its westward side. The strong bottom stress curl on either flank of the jet largely cancels in a zonal integral, but not along a closed streamline, since its opposing signs are in waters of either subtropical or subpolar origin (see Figs. 4b,d). Thus, the integral constraints (6) and (8) provide a geometrical constraint on the flow, which is satisfied through the positioning and orientation of the jet.

3. Channel circulations

In the gyre models the depth-integrated flow is steered by the topography and influences where frictional effects are experienced both in the BV and PV balances. This provides an interesting illustration of how the need to satisfy the two integral constraints can lead to a strong constraint on the geometry of the flow. In many realistic circumstances, the flow interaction with topography is not constrained to occur only in a single western boundary region at each latitude. A wider range of possible interactions with topography may reduce the dynamical constraint and permit a wider range of possible flow types to occur. For this reason we consider a channel flow, with topography in two longitude ranges, to investigate how the circulation is controlled by the topography, and how this influences the PV balance with this more complex topography.

a. Model configuration

The model is set up in a reentrant channel with an idealized topography for the Pacific sector of the Antarctic Circumpolar Current (Fig. 5a), which consists of a barrier with a gap representing Drake Passage and

submerged topography representing features such as the Pacific Rise. The channel extends for 20° latitude by 90° longitude and grid size 1/6° with three layers in the vertical and potential densities (referenced to a depth of 2 km) of 1036.3, 1038.2, and 1038.5 kg m⁻³. The layer interfaces are initially at depths of 1700 and 3500 m, apart from where they intercept topography. The interfaces are such that there are gaps in both the submerged and barrier topography where the interior layer does not initially intercept the topography. Again there is no diabatic forcing included so that changes in PV are due to frictional forcing only. The zonal wind stress,

$$\tau_w^x = \tau_0 \cos[\pi(y + 55)/20], \quad -65^\circ \leq y \leq -45^\circ, \quad (9)$$

is applied to the top layer with wind strengths of $\tau_0 = 0.01, 0.05,$ and 0.2 Pa ($1 \text{ Pa} = 1 \text{ N m}^{-2}$). The bottom friction is again applied over the bottom 10 m with a standard drag coefficient of $c_D = 3 \times 10^{-3}$. The boundary conditions are of no slip, such that \mathbf{u} and $\nabla^2 \mathbf{u}$ are zero on all boundaries.

The models are integrated to a statistically steady state with time-averaged diagnostics then taken over 5 yr. With the strong and intermediate wind strengths the models are integrated in total for 30 yr, while with the weak wind stress the model takes longer to spin up and is therefore integrated for 50 yr. Momentum is transferred vertically from the surface Ekman layer through the water column through a combination of standing and transient eddies to the top of submerged topographic features (Döös and Webb 1994; Wolff et al. 1991). Most of this transfer occurs over and downstream of topographical features (Gille 1997; Hallberg and Gnanadesikan 2001).

An increase in the eastward wind stress, from $\tau_0 = 0.01, 0.05,$ to 0.2 Pa, leads, as expected, to an increase in zonal transport (Figs. 5b–d). With the weakest wind, the flow is predominantly zonal with oscillations (or standing eddies) occurring downstream of topographical features. As the wind strength increases, there are greater deviations of the streamlines over the submerged topography and an increased meridional extent of the boundary current downstream of the barrier. For a greater wind forcing, there is an increased influence of f/H contours as opposed to f contours because of the increased vertical penetration of the current. This penetration is also controlled by the stratification that acts to shield the flow from topography and reduce the influence of f/H contours (Marshall 1995). The f/H contours mainly follow depth contours (Fig. 5a) over the topography and latitude lines between.

Away from the jet, gyres are formed between the

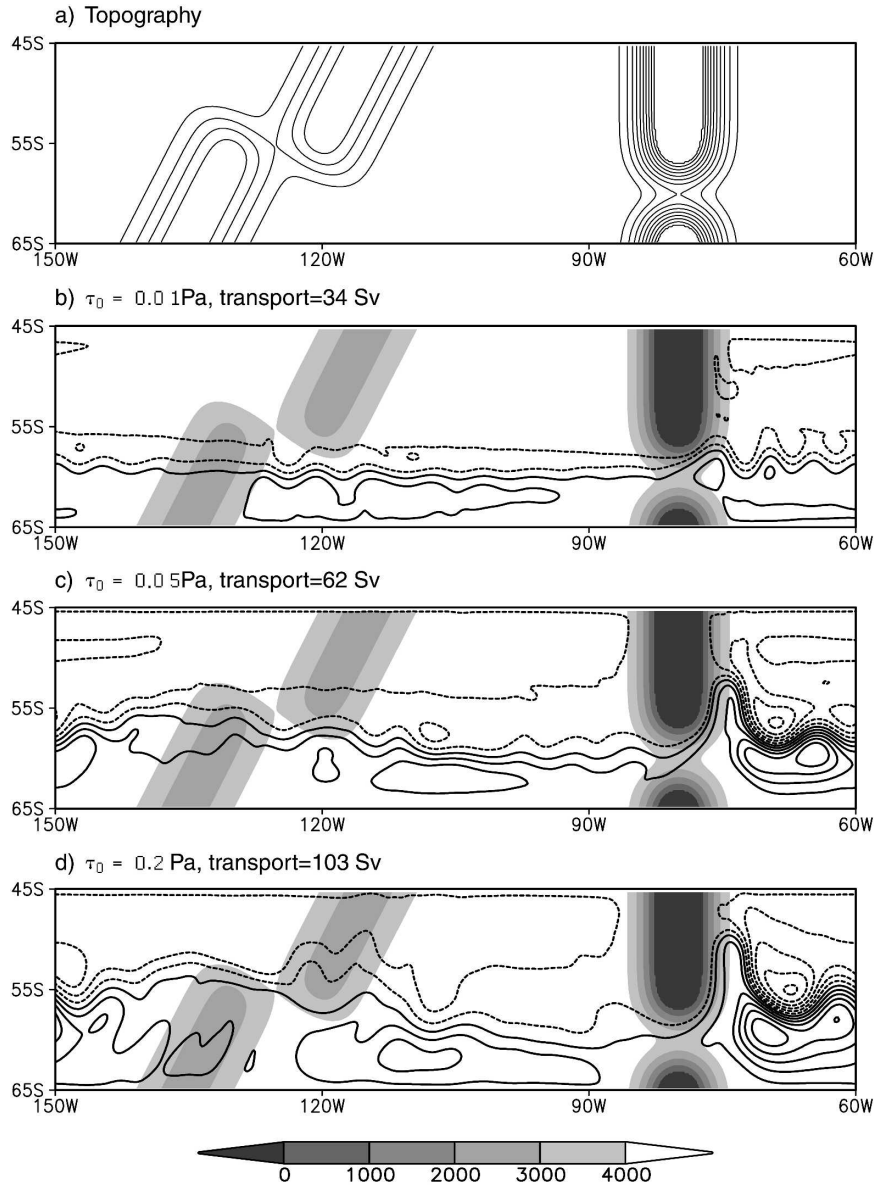


FIG. 5. Maps for the idealized Southern Ocean sector showing (a) the topography with a 500-m contour interval and (b)–(d) the streamfunction for model integrations with increasing surface wind stress from $\tau_0 = 0.01, 0.05$, to 0.2 Pa ; the interval between the streamlines is 10 Sv in (b), 20 Sv in (c), and 40 Sv in (d); depth contours (m) are shaded.

topographic barriers, especially south of the channel (Figs. 5c,d). These gyres form in both subregions of the channel, suggesting that the submerged topography is acting as a barrier to the depth-integrated flow.

b. Does the form stress balance the wind stress zonally?

The depth-integrated pressure gradient exerts a force on the depth-integrated fluid given by

$$\int_{-H}^{\eta} \nabla p \, dz = \nabla P - p_b \nabla H, \quad (10)$$

where the first term on the right-hand side is the horizontal pressure force on the fluid column exerted by the adjacent fluid and the second term is the horizontal component of the normal pressure force above sloping topography. Although both pressure gradient terms in Eq. (10) apply a force on the water column, only the second term on the right-hand side exerts a torque,

referred to as the bottom pressure torque. The stress applied by the integral of the second term across a topographical feature is referred to as form stress and exerts a force on the water column due to the pressure differences across a ridge. The importance of form stress in balancing momentum input by wind stress was predicted by Munk and Palmén (1951), and has since been confirmed by various model studies (Wolff et al. 1991; Gille 1997) and by satellite and in situ data measurements (Morrow et al. 1994; Bryden and Heath 1985).

To identify the role of the form stress, consider the terms in the depth-integrated momentum balance,

$$f\mathbf{k} \times \mathbf{U} = -\nabla P + p_b \nabla H + \boldsymbol{\tau}_w - \boldsymbol{\tau}_b + \mathbf{A}, \quad (11)$$

where the depth-integrated horizontal pressure gradient has been split into two terms on the right-hand side as in Eq. (10). Integrating the eastward component of Eq. (11) along a latitude line around the reentrant channel and scaling with the magnitude of the wind stress τ_0 provides

$$\frac{1}{\tau_0} \oint_{\text{const}f} \left(p_b \frac{\partial H}{\partial x} + \tau_w^x - \tau_b^x + A^x \right) dx = 0, \quad (12)$$

where the first term on the left-hand side is the form stress and superscripts in x denote the eastward component.

In the model integrations, there is the classical balance between the wind stress and form stress integrated around the channel,

$$\oint p_b \frac{\partial H}{\partial x} dx$$

(Fig. 6a; full and dashed lines). Nonlinear effects only augment the contribution of the wind stress in central latitudes. This overall balance between wind stress and form stress implies that the northward Ekman flow driven by wind stress in the top layer is returned southward at depth as a geostrophic flow balanced by pressure differences (form stress) across the topographical features. For the low and high wind stress integrations, the main difference in the momentum balance is that there are sharper changes in both nonlinear and form stress terms north of the gap in topography for the integration with weak wind stress (Fig. 6a). The bottom friction is also slightly larger for a strong wind stress since the jet penetrates deeper into the water column and, hence, interacts more with the ocean bottom.

To identify which topographic features contribute to the form stress, we separate the zonally integrated diagnostics for the form stress into two regions over the submerged topography (between 150° and 95°W) and

over the barrier (between 95° and 150°W); at these domain boundaries, the depth is close to the interior value of 5000 m, although a slight difference over the north side of the channel causes a large difference in form stress, so the separate contributions are not plotted there.

In both wind-forcing cases, the form stress is mainly provided by the barrier region north of the gap (Fig. 6b). For the low wind case, the form stress is mainly concentrated on the northern edge of the gap, but the submerged topography does provide the dominant contribution south of the gap (Fig. 6b; dashed line). In the strong wind case, as the flow through the gap becomes stronger, the jet penetrates deeper and interacts more with the topography of the gap, causing a greater form stress there (Fig. 6b, right panel). However, these contributions to the form stress are difficult to relate to the detailed flow patterns since there are large, partially opposing contributions from the form stress and the gradient of the depth-integrated pressure in Eq. (11) when considering partial zonal integrals.

c. The barotropic vorticity balance

HdC discuss the connection between form stress and bottom pressure torque. They show that, if the depth and zonally integrated momentum equation involves a balance between the wind stress and form stress at each latitude, then for the BV equation there is a corresponding balance between the wind stress curl and the bottom pressure torque when integrated over a zonal strip.

Consequently, given the importance of the form stress in our model diagnostics for Eq. (12), we now consider the associated role of the bottom pressure torques in the BV Eq. (2). The bottom pressure torques are linked to form stress in an integral sense, where integrating along a latitude line around the channel provides

$$\frac{\partial}{\partial y} \oint p_b \frac{\partial H}{\partial x} dx = - \oint J(p_b, H) dx \quad (13)$$

so that meridional gradients in the form stress in Eq. (12) are connected to the line integral of bottom pressure torque.

To identify the contribution of the different terms in Eq. (2), each of the terms is integrated around the basin and scaled with the magnitude of the wind stress τ_0 to give

$$\frac{1}{\tau_0} \oint [-\beta V + J(p_b, H) + \mathbf{k} \cdot \nabla \times (\boldsymbol{\tau}_w - \boldsymbol{\tau}_b + \mathbf{A})] dx = 0. \quad (14)$$

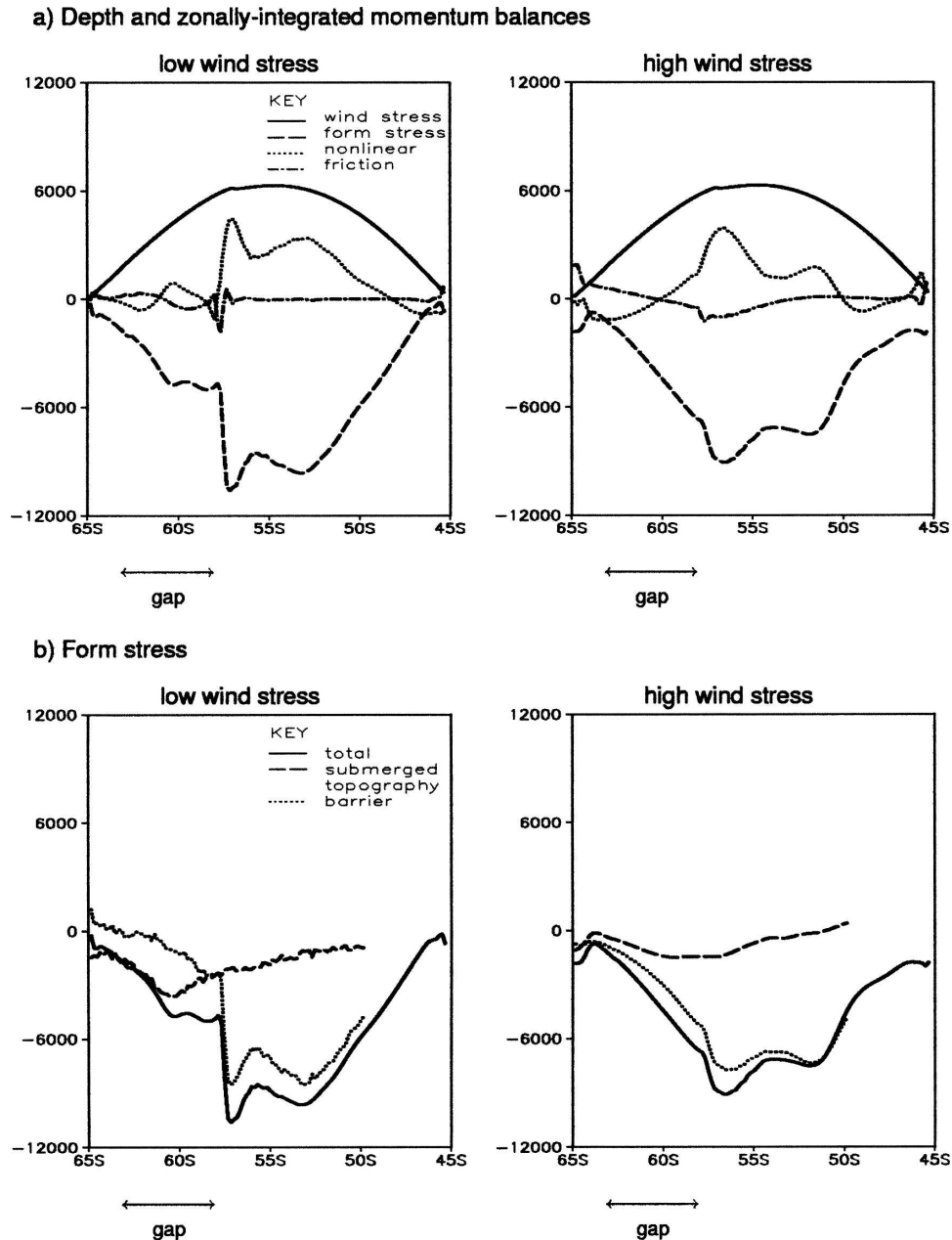


FIG. 6. (a) The depth and zonally integrated momentum balances integrated around the channel (scaled by the wind stress τ_0 ; 10^3 m) for model integrations with (left) weak and (right) strong wind stress. The wind stress (solid line) is primarily balanced by the form stress (dashed line) with the remainder balanced by the nonlinear terms (dotted line) and a small frictional contribution (dash-dot line). (b) The form stress variation across the channel (solid line) including the separate contributions over the barrier region (dotted line) and submerged topography (dashed line); the separate contributions are not plotted north of 50°S.

The integral diagnostics are performed over 3.7°-wide latitude bands (depicted in Fig. 7a) for the low wind stress integration, and data within 0.8° of the northern and southern boundaries is ignored since the lateral boundary conditions become important there. Over

latitude bands spanning the domain, βV integrates to zero since there is no overall mass flux. The bottom pressure torque (gray bars) balances opposing contributions from the wind stress curl (white bars) and nonlinear terms (black bars) (Fig. 7b). The wind stress curl

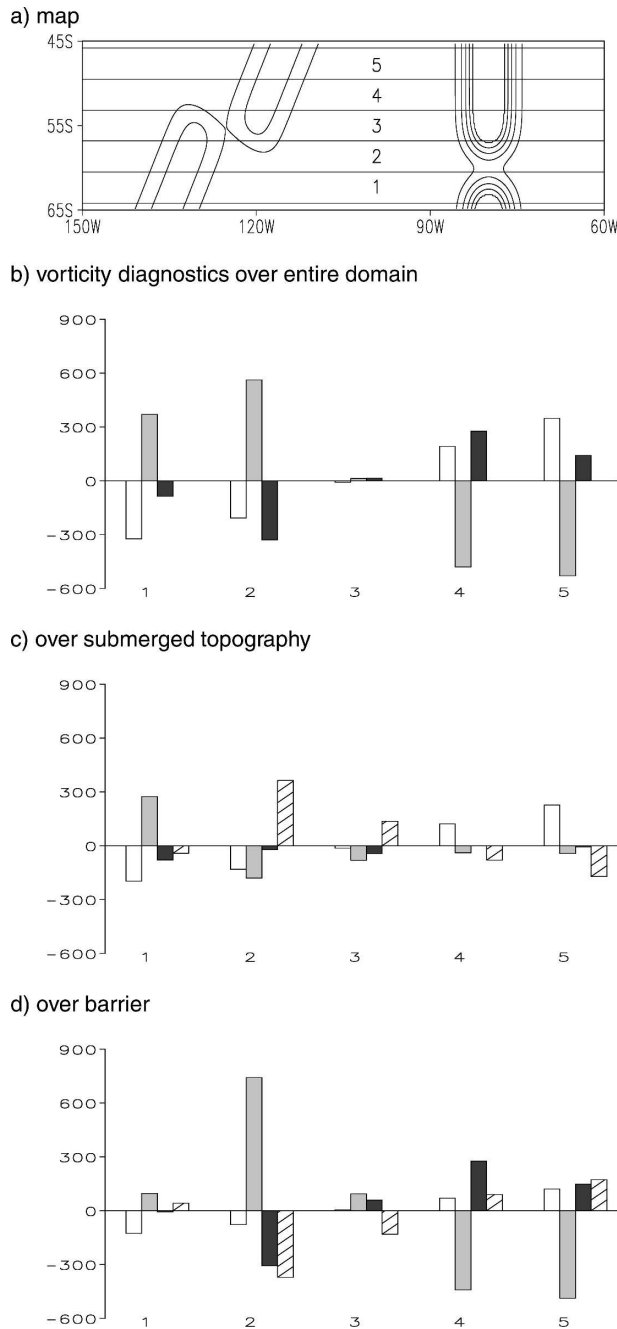


FIG. 7. The barotropic vorticity balances for the weak wind stress integrated over zonal strips (scaled with τ_0 ; 10^4 m): (a) map of the domain with the topography (contour interval 1000 m) and the five latitude bands used in the zonal integrals; the vorticity balance over each latitude band for (b) the entire channel and (c) separately for the submerged channel and (d) for the barrier. Over the entire channel, the wind stress curl (white bar) is balanced by the bottom pressure torque (gray bar) and augmented by the nonlinear terms (black bar). Over the separate regions, the vorticity forcing leads to a resultant meridional flow, $-\beta V$, given by the hatched bar.

inputs positive and negative vorticity north and south of the channel, respectively, which is generally augmented by the nonlinear terms.

The BV balances are now separately considered in regions either including the submerged topography or the partial barrier, with domain boundaries again defined at 95° and 150° W (Figs. 7c,d). North of the channel (regions 4 and 5), there are wind-driven gyres with the wind stress curl driving a northward flow (hatched bar) over the submerged topography (Fig. 7c), which is returned southward by bottom pressure torques over the barrier (Fig. 7d). South of the channel (region 1), the gyre balance again occurs with the wind stress curl driving a southward flow that is returned by the bottom pressure torque. In this latter case, though, bottom pressure torques occur over both sections of topography. Across the gap in the barrier (region 2), there is a large bottom pressure torque permitting a northward flow (Fig. 7d; gray bar), which is associated with the sharp gradient in form stress at the northern edge of the gap (Fig. 6b; low wind stress). This strong northward transport downstream of the barrier is eventually returned southward through the combination of the wind stress curl over the rest of the channel, the nonlinear terms over the barrier, and the bottom pressure torque over the submerged topography (Figs. 7c,d).

d. What is the local role of bottom pressure torques?

The bottom pressure torque acquires a characteristic pattern over the topography in the channel, similar to that seen in the basin. In the channel, downstream of the submerged topography, there is a wind-driven gyre in the south with the northward return flow in the western boundary associated with the positive bottom pressure torque (Fig. 8). At the same time, farther north, there is an accompanying negative bottom pressure torque associated with a southward deflection of the zonal jet. This dipole pattern of positive and negative bottom pressure torque is a consequence of the form stress, first decreasing northward along the topography and then increasing back to zero (Fig. 6b; low wind stress). This balance can be argued more formally by considering the area integral of the bottom pressure torque over an area contained by a depth contour H , where

$$\int J(p_b, H) dA = H \oint_{\text{const } H} \nabla p_b \cdot ds = 0, \quad (15)$$

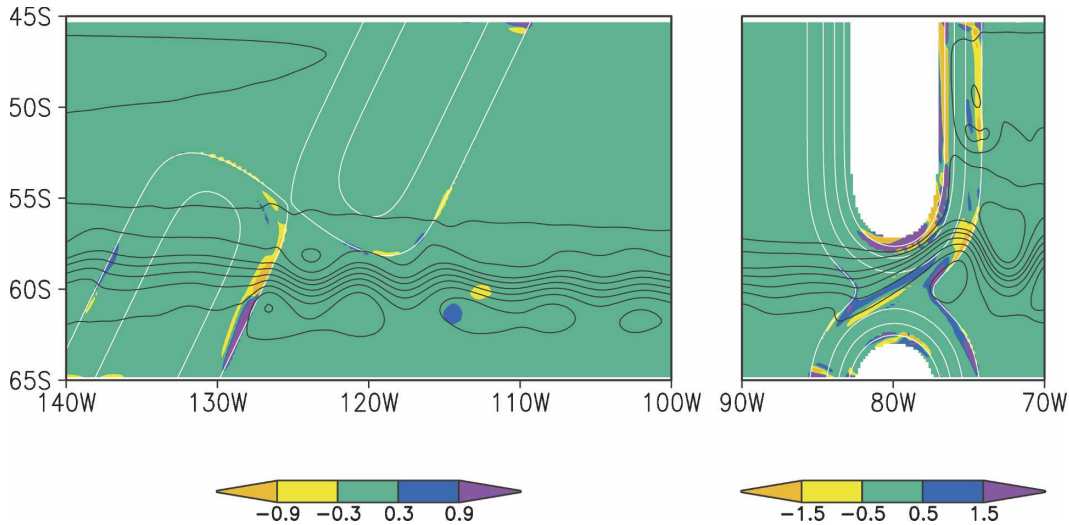


FIG. 8. Bottom pressure torque (colored, scaled with τ_0 ; 10^{-4} m^{-1}) (left) over the submerged topography and (right) through the gap in the barrier; streamlines are marked by black contours with an interval of 10 Sv and the white contours show the position of the depth contours (1000 m). Note how, over the submerged topography, the bottom pressure torque leads to a northward return flow for the southern gyre as well as inducing a southward deflection of the zonal jet.

and hence this area integral between two depth contours is zero. While the model topography does not have a suitable H contour to integrate around (Fig. 5a), we can consider the modified situation where the southern boundary is artificially shifted southward into a region of no wind forcing and the depth contours close there. Now integrating around the closed H contours around the submerged island, the integrated bottom pressure torque has to be zero, which implies that a positive bottom pressure torque has to be offset by a negative bottom pressure torque along the same H contour, consistent with the dipole pattern in bottom pressure torque seen in Fig. 8. It is interesting that this dipole pattern continues to occur, even in the current case in which the two topographic obstacles are connected by a depth contour. This dipole pattern implies that the southward deflection of the jet is the result of bottom pressure torque transferring BV from the gyre circulation (where the BV input occurs from wind stress curl) to the jet.

Over the barrier region, for weak wind stress, there is a very finescale, complicated pattern of bottom pressure torques with the largest torques concentrated at the edge of the barrier (Fig. 8, right panel; Fig. 9a). Southward flow in a western boundary current along the barrier (45°–55°S) is associated with the large negative bottom pressure torque at the edge of the barrier. This negative torque is linked by the integral constraint (15) to a strong positive torque at the edge of the barrier (~57°S) balancing a northward flow through the gap.

As the wind strength increases, there is a stronger northward deflection of the jet (Figs. 9a–c). Regions of positive and negative bottom pressure torque develop farther down the slope of the barrier because of a greater interaction of the flow with the deep topography. In the zonal integral, these downstream regions become as important as the thin bands of bottom pressure torque on the edge of the barrier; consequently there is a smoother meridional transition in form stress gradients (Fig. 6). With greater wind stress, there is also a shift of the gyre return flow north of the jet from the edge of the barrier farther off the slope (Fig. 9). It is unclear whether the bottom pressure torques are acting to transfer vorticity in the same way as for the weaker flow, although there are undoubtedly positive torques associated with a northward flow through the gap and both positive and negative torques associated with a meridional flow downstream.

In summary, the bottom pressure torque provides a mechanism to return the interior flow of a wind-driven gyre, either within a basin or a channel with topographical barriers (Fig. 10). The bottom-pressure torque has a characteristic dipole pattern. Within a channel, the integral effect of the bottom pressure torque is to transfer vorticity from the wind-driven gyre into the jet leading to a meridional deflection in the jet. As the wind forcing increases and the jet becomes stronger, this process may weaken as the nonlinear term strengthens and transient eddies become an alternative mechanism to transfer vorticity.

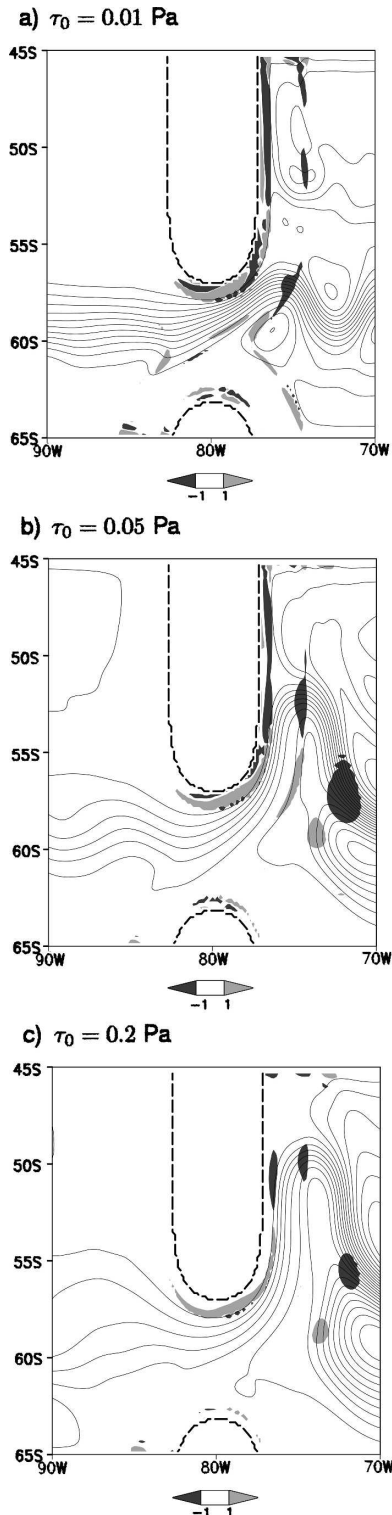


FIG. 9. Bottom pressure torque (shaded, scaled with τ_0 ; 10^{-4} m^{-1}) at the barrier for (a) weak, (b) moderate, and (c) strong wind stress; streamlines are plotted with full contours with intervals of (a) 3, (b) 10, and (c) 20 Sv, and the edge of the topography is marked by dashed lines. Note how the northward deflection of the jet downstream of the gap increases with the wind stress.

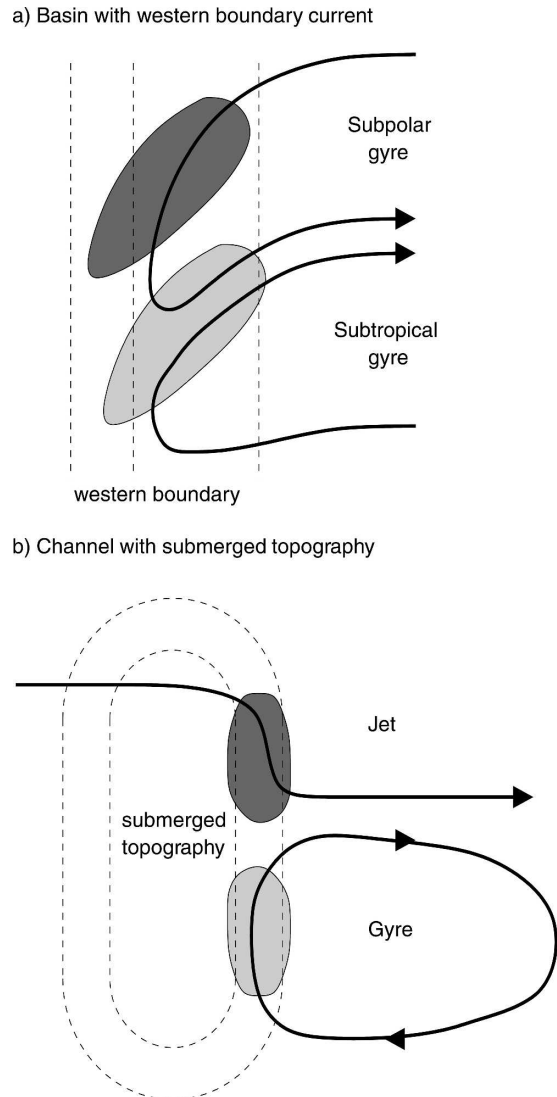


FIG. 10. A schematic figure depicting the pattern of the bottom pressure torque (shaded) for (a) a basin and (b) a channel with submerged topography; streamlines and depth contours are full and dashed contours, respectively. In both cases, the bottom pressure torque enables a return flow along the sidewall of the western boundary of the gyre. In the channel, the bottom pressure torque transfers vorticity from the wind-driven gyre to the jet, which leads to a downstream displacement in the position of the jet.

4. Potential vorticity balance

The PV balances are now considered in more detail, given how unimportant frictional forces appear to be in the BV budget. For a steady state, there is an integral balance between sources and sinks of PV from the curl of frictional forces within a closed layer streamline as in Eq. (6). For a statistically steady state, eddy stirring can become important in transferring PV across the time-mean streamlines between regions of opposing PV sources and sinks.

The pattern of the frictional forcing for a shielded layer depends principally on the position of the jets, which in turn are affected by the bottom pressure torque. Given this connection, we now explore how the frictional forcing of PV occurs in a shielded layer: first, within a basin and, second, within a channel with partial barriers.

a. Gyre response

The gyre response to frictional sources of PV is addressed in idealized isopycnic model studies by Hallberg and Rhines (2000) and Williams and Roussenov (2003). The wind forcing is confined to a surface layer, and interior, shielded isopycnic layers only experience a forcing from bottom stress or lateral (eddy) diffusion.

Following Williams and Roussenov (2003), for these shielded layers, bottom friction is only important along sloping sidewalls where the circulation interacts with topography. Bottom friction therefore acts to oppose the background circulation induced by the wind forcing and leads to bands of high PV on the western side of the subtropical gyre and low PV on the western side of the subpolar gyre (Fig. 11; dark and light shading). These contrasts in PV are advected toward the midbasin separated jet, where a PV front is created. However, rather than resulting in a strong PV contrast between the gyres, this PV front is eroded in the interior jet by an active eddy circulation that acts to homogenize PV over much of the layer.

In the gyre experiments, the frictionally induced bands of high and low PV along the western boundary are confined within different time-mean streamlines residing either within the subtropical or subpolar gyres. Consequently, unless there is opposing frictional forcing, eddy stirring is required to provide a flux of PV from one gyre to another in order to attain a steady state.

b. Channel response

1) HOW DOES THE PV BUDGET BALANCE WITHIN THE CHANNEL?

The channel is divided into two basins by partial topographical barriers, with the jet connecting the two basins; for PV experiments for a basin with a partial inflow, see also Yang and Price (2000). Unlike the gyre case, it is now possible for a single streamline in the interior layer to pass over both partial barriers and, in moving both northward and southward, experience two regions of frictional forcing with different signs. As these two regions are widely separated in longitude, this can influence the large-scale PV distribution in the

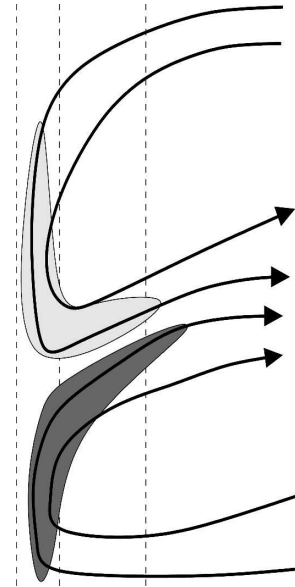


FIG. 11. A schematic figure depicting the different potential vorticity distributions within a double-gyre basin with sloping sidewalls; streamlines and depth contours are full and dashed contours, respectively. Along the sloping sidewall, bottom friction leads to inputs of high (dark) and low PV (light) along the western flanks of the subtropical and subpolar gyres; note that the high PV singularity along the western edge of the domain is not shown where the layer thickness vanishes. The resulting PV contrast is advected into the interior by the separated jet. However, an active baroclinic eddy circulation can erode this PV contrast (Williams and Roussenov 2003).

layer. This PV distribution is considered in the model run with largest wind stress since eddy homogenization is greatest in this case.

To see how this PV change is achieved, it useful to separate the flow into “open” Montgomery M contours passing through the gaps in topography and encircling “Antarctica” and “closed” M contours that remain within a single basin in the shielded layer; $M = P/\rho + gz$, where P is the pressure and z is the height of the density interface. For example, consider the open M contour passing through both basins, which is close to the southern wall at 140°W in Fig. 12a. This M contour passes through regions of different frictional forcing close to the topographic barriers leading to regions of low PV ($130^\circ\text{--}90^\circ\text{W}$), as well as high PV ($80^\circ\text{--}145^\circ\text{W}$), where high PV is defined as being more positive. Now, consider the closed M contours centered at 60°S , 110°W or 60°S , 65°W , which remain relatively far from regions of frictional forcing alongside the topography. These closed M contours enclose regions with a single value of nearly uniform PV. The particular PV value taken up within the closed M contour is determined by the eddy transfer from the neighboring open M contour, in ac-

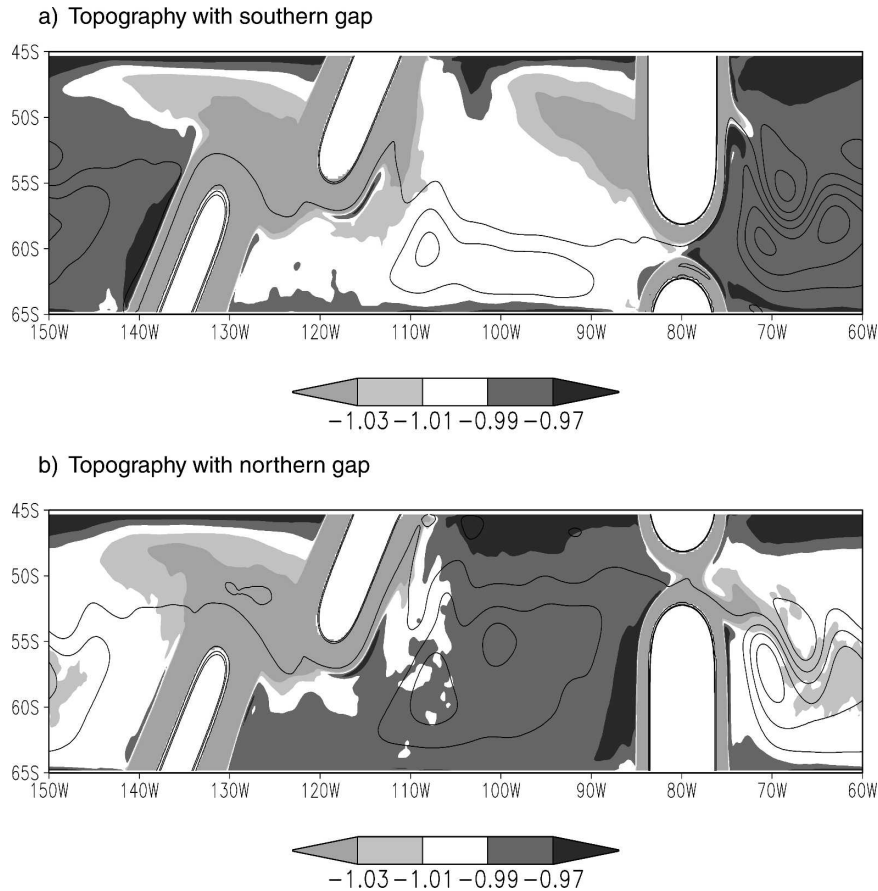


FIG. 12. Time-averaged potential vorticity (shaded) with Montgomery contours ($\text{m}^2 \text{s}^{-2}$) for the shielded, intermediate layer for (a) original topography with a southern gap and (b) topography with a northern gap in the barrier. The PV is scaled in terms of the magnitude of the background PV, $[(f + \zeta)/h](h_o/f_o)$, where f_o is the value of f at latitude 55°S and h_o is the initial layer thickness away from the topography. Note how the time-averaged PV acquires a different distribution within each subbasin with the more positive PV (dark) occurring upstream of the northern gap in the topography.

cord with the Rhines and Young (1982) view of eddy homogenization.

2) WHY IS THERE A DIFFERENT PV EVOLUTION WITHIN EACH SUBBASIN?

From the model results we see a different PV evolution over the southern half of each of the subbasins: lower and higher PV upstream and downstream of the gap in the barrier respectively (Fig. 12a). As the model is initialized with uniform thickness over the layer (except where it intersects topography), the PV is initially higher in the northern gap in the submerged topography and is lower in the southern gap in the barrier because of differences in the planetary vorticity. Consequently, in a statistically steady state, fluid can only recirculate around the channel if either (i) the initial PV contrast is eroded or (ii) the PV sources and sinks ad-

just to provide the necessary PV input for fluid to pass from one subbasin to the other.

The different PV response in the two subbasins appears to reflect the different initial contrasts in the PV in the gaps between the barrier and submerged topography. Our experiment suggests that the frictional sources of PV are providing overall positive inputs upstream of the submerged topography (with the gap farther north) and negative inputs upstream of the partial barrier (with the gap farther south). Consider a statistically steady state where the PV contrast between the gaps has not been eroded: A streamline that has just passed through the gap in the submerged topography must decrease its PV in order to pass through the gap in the barrier at a lower latitude. It experiences negative frictional forcing on the western boundary of the basin creating a plume of low PV, which is advected into the

basin and mixed by eddy stirring. Having passed through the gap in the barrier the flow must then experience positive forcing to increase its PV. The amount of frictional forcing in each basin has adjusted to allow a recirculation through the channel in the same way that the frictional forcing in a wind-driven gyre adjusts to balance the wind forcing in a statistically steady state.

To test whether the latitude of the gaps is important, we conduct an additional experiment with the same submerged topography but with the gap in the barrier shifted northward. In this case, the PV evolves to a contrasting state with higher and lower values upstream and downstream of the northern gap in the barrier, in accord with our hypothesis (Fig. 12b). The latitude of the gaps in the topography does appear to be the controlling factor in these two experiments rather than subtle differences between the submerged topography and the barrier (which differ in orientation and depth range) or boundary effects.

This response is consistent with the view that the PV sources and sinks adjust according to the PV contrast between the gaps in the topography. In both experiments, eddy stirring is effective in eroding contrasts in PV within each basin, but is ineffective in removing contrasts between the basins.

3) HOW ARE THE CHANGES IN PV ACHIEVED?

To confirm the picture deduced above, the PV budget has been calculated in a Lagrangian frame following time-mean streamlines. Results from a particular streamline are presented here to illustrate the main processes.

Since a time-mean streamline is followed, the PV balance Eq. (1) is written to include an explicit eddy transfer of PV anomalies: the Lagrangian change in time-averaged PV depends on the forcing from frictional torques and the eddy advection of PV anomalies,

$$\frac{D\bar{Q}}{Dt} = -\frac{1}{h} \mathbf{k} \cdot \nabla \times \frac{\tau_b}{\rho h} - \overline{\mathbf{u}' \cdot \nabla Q'}, \quad (16)$$

where Q is the PV, the overbar represents an Eulerian time average, and a prime represents a temporal deviation; $D/Dt = \bar{\mathbf{u}} \cdot \nabla$ is the Lagrangian rate of change following the time-mean flow. The eddy transfer of PV, $\overline{\mathbf{u}' \cdot \nabla Q'}$, is diagnosed at each grid point from the model diagnostics over a 5-yr time average.

A Lagrangian trajectory is considered lasting 400 days following a time-mean streamline passing close to the barrier with the southern gap (Fig. 13a; full line) and experiencing frictional forcing along the downstream side of the barrier (Fig. 13a; shading). For this

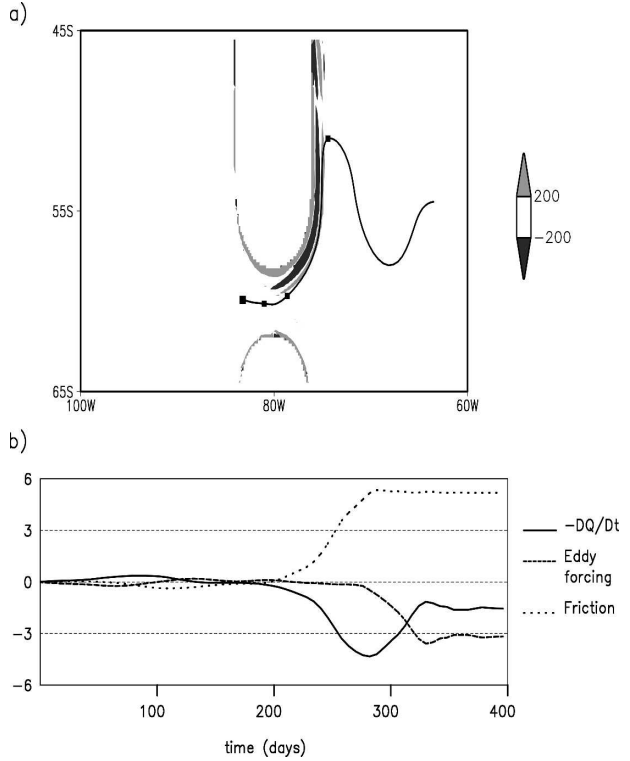


FIG. 13. Potential vorticity balance following a Lagrangian time-mean trajectory passing through the gap in the barrier within the interior layer. (a) Map of the frictional forcing (shaded, $10^{-18} \text{ m}^{-1} \text{ s}^{-2}$) with the Lagrangian track overlaid in black with markers every 100 days. (b) Terms from the PV balance are plotted as running integrals ($10^{-13} \text{ m}^{-1} \text{ s}^{-1}$) against time (days) along the trajectory for $-DQ/Dt$ following the time-mean flow (solid line), eddy forcing ($\overline{\mathbf{u}' \cdot \nabla Q'}$) (dashed line), and frictional forcing (dotted line). Note how the bottom friction leads to an increase in PV alongside the barrier (after day 200), which is partly eroded by eddy forcing in the interior (after day 280).

region, there is a downstream increase in the background PV (Fig. 12a). Along the Lagrangian trajectory, this increase in PV is achieved through bottom friction providing a positive input of vorticity (after day 200 in Fig. 13b; full and dotted lines). However, when the trajectory leaves the side of the barrier (after day 280), the eddy forcing opposes this frictional input of PV. For this particular trajectory, the frictional input of PV dominates over the eddy transfer, leading to an overall Lagrangian increase in PV. In neighboring trajectories the PV is not increased directly by friction, but by the eddy forcing transferring PV. While the detailed balances between the frictional and eddy forcing is highly sensitive to the particular trajectory, this Lagrangian example illustrates how the systematic evolution in the PV (Fig. 12) is controlled by a competition between the frictional sources of PV and eddy stirring (Hallberg and Rhines 2000; Williams and Roussenov 2003).

5. Discussion

This study addresses two questions: 1) How are the BV and PV balances reconciled in simple ocean geometries and 2) is the role of bottom pressure torque simply to steer the flow or does it have a broader (perhaps indirect) dynamical influence on the flow?

The first question is most clearly addressed by the gyre experiments. These show the development of a dipole in bottom pressure torque (Fig. 10a), removing BV from the subpolar gyre latitudes and adding BV to the subtropical gyre latitudes to balance the wind stress curl in those regions. Friction is unimportant in this balance, but is central to the PV balance of the wind-forced layer if the eddy forcing is small. This PV balance, however, is an integral constraint on closed mean streamlines, which can change path to accommodate the forcing. The balance between the meridional flow and bottom pressure torque results in the streamlines broadly following f/H contours. This leads to a separation of the flow from the boundary in a jet, which allows the two constraints to be consistently satisfied: the water to the left of the jet center can be part of the subpolar gyre and water to the right can be part of the subtropical gyre. Friction then acts in the correct sense to balance the PV budget of each gyre, but the bottom stress curl cancels out when integrated across the jet. As the flow becomes more nonlinear, eddy transfer of PV across the jet starts to reduce the role of bottom friction in this balance.

The more complicated geometry of the channel with topography in two longitude ranges makes a wider range of bottom pressure torque distributions possible. However, the dipole pattern in bottom pressure torque along a boundary remains, as seen in the gyre experiment (Fig. 10a), and is a consequence of the constraint that the bottom pressure torque must integrate to zero over any region bounded by depth contours. The bottom pressure torque on each piece of topography is intimately related to the associated form stress, but the resulting flow patterns are more clearly related to bottom pressure torque than to form stress. To the north of the central jet, there is a gyre circulation closed by a western boundary current against the partial barrier. The bottom pressure torque in this boundary current balances the positive wind stress curl over this region. South of the jet gyres occur within each of the basins, with negative wind stress curl driving southward flow in the gyre interiors and with a return northward flow over the topography balanced by bottom pressure torque (Fig. 10b). Since the bottom pressure torque occurs in a dipole along the topographic obstacle, the input of BV from the wind curl is effectively transferred

from the gyre regions to the jet, which undergoes meridional deflections as the jet passes over the topography.

For the gyre cases, the interaction of the jet with topography does not have a large-scale effect on the PV distribution. While separation of the current from the boundary leads to a front between water of subpolar and subtropical origin (Becker and Salmon 1997), this front and vorticity contrast does not penetrate far into the interior if there is strong eddy mixing (Williams and Roussenov 2003). In contrast, for our channel cases, there are large-scale changes in PV arising from the frictional torques along the submerged topography. This frictional forcing is associated with topographical deflections of the jet, achieved by bottom pressure torques. The frictional forcing alters the PV of the jet, enabling the jet to pass through topographic gaps at different latitudes, and eddy mixing then spreads this longitudinal PV contrast into the gyres.

In summary, bottom pressure torques are crucial in steering jets and in returning western boundary flows in gyres. In turn, the topographic steering dictates where the bottom friction is important in our model, which affects the PV distribution and allows a closed circulation. The geometry of the jet is controlled by having to satisfy the contrasting integral constraints for BV and PV: friction is unimportant in a zonal integral for BV, but is important for an area-integral within a closed streamline for PV. While our model studies use idealized closures for the bottom friction and viscous diffusion, we expect our main conclusions to carry over for more realistic closures, but not necessarily the detailed patterns for bottom pressure torque and bottom friction. Despite the importance of bottom pressure torques in steering the flow, they are difficult to diagnose observationally because of the finescales of the topography and small pressure differences involved, and in practice they may remain an important mechanism that has to be diagnosed from circulation and inverse models.

Acknowledgments. The work was supported by a U.K. NERC studentship (NER/S/A/2000/03857) and NERC RAPID grant (NER/T/S/2002/00439), as well as by the Proudman Oceanography Laboratory. We are grateful to Vassil Roussenov for assistance with the modeling experiments. We also thank the editor Eric Firing and two anonymous referees whose comments led to a substantial improvement in the paper.

REFERENCES

- Becker, J. M., and R. Salmon, 1997: Eddy formation on a continental slope. *J. Mar. Res.*, **55**, 181–200.

- Bleck, R., and L. T. Smith, 1990: A wind-driven isopycnic coordinate model of the North and equatorial Atlantic Ocean. 1. Model development and supporting experiments. *J. Geophys. Res.*, **95**, 3273–3285.
- Bryden, H. L., and R. A. Heath, 1985: Energetic eddies at the northern edge of the Antarctic Circumpolar Current in the southwest Pacific. *Progress in Oceanography*, Vol. 14, Pergamon Press, 65–87.
- Döös, K., and D. J. Webb, 1994: The Deacon cell and the other meridional cells of the Southern Ocean. *J. Phys. Oceanogr.*, **24**, 429–442.
- Fofonoff, N. P., 1954: Steady flow in a frictionless homogeneous ocean. *J. Mar. Res.*, **13**, 254–262.
- Gille, S. T., 1997: The Southern Ocean momentum balance: Evidence for topographic effects from numerical model output and altimeter data. *J. Phys. Oceanogr.*, **27**, 2219–2232.
- Hallberg, R., and P. B. Rhines, 2000: Boundary sources of potential vorticity in geophysical circulations. *Developments in Geophysical Turbulence*, R. M. Kerr and Y. Kimura, Eds., Kluwer, 51–65.
- , and A. Gnanadesikan, 2001: An exploration of the role of transient eddies in determining the transport of a zonally reentrant current. *J. Phys. Oceanogr.*, **31**, 3312–3330.
- Holland, W. R., 1973: Baroclinic and topographic influences on the transport in western boundary currents. *Geophys. Fluid Dyn.*, **4**, 187–210.
- Hughes, C. W., 2000: A theoretical reason to expect inviscid western boundary currents in realistic oceans. *Ocean Modell.*, **2**, 73–83.
- , and B. A. de Cuevas, 2001: Why western boundary currents in realistic oceans are inviscid: A link between form stress and bottom pressure torques. *J. Phys. Oceanogr.*, **31**, 2871–2885.
- Marshall, D. P., 1995: Influence of topography on the large-scale ocean circulation. *J. Phys. Oceanogr.*, **25**, 1622–1635.
- Morrow, G., R. Coleman, J. Church, and D. Chelton, 1994: Surface eddy momentum flux and velocity variances in the Southern Ocean from *Geosat* altimetry. *J. Phys. Oceanogr.*, **24**, 2050–2071.
- Munk, W. H., and E. Palmén, 1951: Note on the dynamics of the Antarctic Circumpolar Current. *Tellus*, **3**, 53–55.
- Rhines, P. B., and W. R. Young, 1982: Homogenization of potential vorticity in planetary gyres. *J. Fluid Mech.*, **122**, 347–368.
- Stommel, H., 1948: The westward intensification of wind-driven ocean currents. *Trans. Amer. Geophys. Union*, **29**, 202–206.
- Welander, P., 1968: Wind-driven circulation in one- and two-layer oceans of variable depth. *Tellus*, **20**, 1–15.
- Williams, R. G., and V. Roussenov, 2003: The role of sloping sidewalls in forming potential vorticity contrasts in the ocean interior. *J. Phys. Oceanogr.*, **33**, 633–648.
- Wolff, J.-O., E. Maier-Reimer, and D. Olbers, 1991: Wind-driven flow over topography in a zonal beta-plane channel: A quasi-geostrophic model of the Antarctic Circumpolar Current. *J. Phys. Oceanogr.*, **21**, 236–264.
- Yang, J., and J. F. Price, 2000: Water-mass formation and potential vorticity balance in an abyssal ocean circulation. *J. Mar. Res.*, **58**, 789–808.